Detailed structural and electrochemical comparison between a high potential layered P2-NaMnNi- and P2-NaMnNiMg-oxide

Cornelius Gauckler[a¥], Manuel Dillenz[b¥], Fabio Maroni[a], Lukas Pfeiffer[a], Johannes Biskupek[e], Mohsen Sotoudeh[b], Qiang Fu[f], Ute Kaiser[e], Sonia Dsoke[f,g], Holger Euchner[d], Peter Axmann[a], Margret Wohlfahrt-Mehrens[a,c], Axel Groß[b,c], Mario Marinaro[a]*

[a]*ZSW-Zentrum für Sonnenenergie und Wasserstoff-Forschung, Helmholtzstrasse 8, 89081, Ulm, Germany*

[b]*Institute of Theoretical Chemistry, Ulm University, Albert-Einstein-Allee 11, 89081 Ulm, Germany*

[c]*Helmholtz Institute Ulm (HIU) for Electrochemical Energy Storage, Helmholtzstraße 11, 89069 Ulm, Germany,*

[d]*Institute of Physical and Theoretical Chemistry, Universität Tübingen, Auf der Morgenstelle 15, 72076 Tübingen, Germany*

[e]*Central Facility for Electron Microscopy, Ulm University, Albert-Einstein-Allee 11, 89081 Ulm, Germany*

[f]*Institute for Applied Materials – Energy Storage Systems (IAM – ESS), Karlsruhe Institute of Technology, Hermann-von-Helmholtz-Platz 1, 76344 Eggenstein- Leopoldshafen, Germany*

[g]*Helmholtz-Institute Ulm for Electrochemical Energy Storage (HIU), P.O. Box 3640, 76021, Karlsruhe, Germany*

Abstract

Rechargeable sodium-ion batteries are viable candidates as next generation energy storage devices. Nonetheless, the development of high-potential and stable cathode materials is still one among the open tasks. Here we propose a combined experimental/theoretical approach to shed light on the effect of magnesium doping on the layered P2-$Na_{0.67}Mn_{0.75}Ni_{0.25}O_2$ cathode material. The P2-$Na_{0.67}Mn_{0.75}Ni_{0.25}O_2$ baseline material and P2-$Na_{0.67}Mn_{0.75}Ni_{0.20}Mg_{0.05}O_2$, synthesized via co-precipitation route followed by thermal treatment, have been physically and chemically characterized via XRD, SEM and TEM, as well as electrochemically via galvanostatic cycling and GITT. The Mg-doped material showed stabilization of the high potential plateau and improved cycle life. The analysis of the phase transition with synchrotron operando XRD showed, multiple possible intermediate phases ("Z-phase"), rather than a pure OP4 like structure. Based on our experimental data and periodic DFT calculations, phase stabilities of the O2, P2, and OP4 phases for the pristine and Mg-doped systems were investigated to elucidate the origin of the "Z"-phase formation in the Mg-doped material.

Keywords

DFT; Doping; Na-Ion Batteries; *operando*-XRD; P2-layered oxide; phase transition

[¥] both authors equally contributed to the manuscript

[*] *Corresponding author: mario.marinaro@zsw-bw.de*

Introduction

Lithium-ion batteries (LIBs) have conquered the electronics market in the past two decades and attracted worldwide attention.[1] As the need for lithium resources increased, so has the demand for low-cost alternatives. In this context, sodium-ion batteries (SIBs) have gained growing attention due to the abundance of the raw materials, cost-effectiveness, easily accessible as Na_2CO_3 in seawater, and comparable electrochemical potential with redox couple of Na^+/Na versus Li^+/Li (-2.71 V vs. SHE and -3.01 V vs. SHE, respectively).[2] However, the need of high performance cathode materials has limited the commercialization of SIBs so far.[3] In literature, two major cathode material classes have been investigated more intensively, namely polyanion compounds and layered oxides. Among these materials, Na-TM-O (TM=3d transition metal) layered oxides seem to be promising, due to their high energy density and high gravimetric capacity in comparison with polyanion compounds whose energy density and gravimetric capacity are limited due to the presence of heavy and bulky polyanionic groups.[3,4]

Layered oxides can be developed with a wide variety of transition metals and crystallize into several polymorphs depending on the synthesis condition. The most intensively studied materials are the P2- and O3-type layered oxides as described by the Delmas notation.[5] In general, those structures can be described as a stack of MO_2 slabs in which TM cations occupy the interstitials between two hexagonal O planes. The alkali cation (Na^+) resides in between the MO_2 slabs. The letters P and O refer to the coordination environment of sodium cations (P=prismatic; O=octahedral) and the number reflects the number of TM layers per unit cell.[6,7] In comparison, the P2-structure tend to undergo less complex phase transitions, e.g. $Na_{0.67}Mn_{0.67}Ni_{0.33}O_2$ (P2→O2) than O3-type structures, e.g. $NaNi_{0.5}Mn_{0.5}O_2$ (O3→O′3→P3→P′3→P3′′).[8] Additionally, most O3-type $NaTMO_2$ materials seem to be hygroscopic and prone to react with moisture to form amorphous Na_2CO_3.[9] Moreover, P2 structures show higher rate capability and cycling stability, whereas O3 type structures offer higher initial capacity due to the higher Na content.[10]

The choice of transition metals is quite cruicial since it will determine the average potential of the material. In order to achieve high potential cathode materials for SIBs, Mn- and Ni-based layered oxides seem to be a good choice.[11] P2-$Na_{0.67}Mn_{0.67}Ni_{0.33}O_2$ has been studied quite intensively due to its high

theoretical capacity (173 mAh g^{-1}) and its high operating potential (>3.5 V vs Na/Na^+).[6,12,13] However, two major challenges have to be addressed in order to improve the cycling stability: 1) the slower diffusion rate due to Na^+-ion/vacancy ordering, and 2) the P2- to O2-layered oxide phase transition occurring at low Na content (~0.3 Na) / high potential (4.2V).[14] Limiting the lower cut-off potential to 2.00 V (vs. Na/Na^+) can limit the presence of Jahn-Teller active Mn^{3+}, thus also limit the formation of a distorted P'2 phase. Eliminating the formation of a distorted P'2 phase, results in less stress within the material and therefore improves the cycle stability.[15] In a recent work from Gutierrez et al. it was also shown that the low diffusivity from a layered oxide with the ratio of Mn:Ni of 2:1 can be highly improved by increasing the Mn content and changing the ratio to 3:1 (Mn:Ni) and resulting in reduced charge ordering with less pronounced Na^+/vacancy ordering.[6]

In this work, the major focus is to subdue the P2-O2 phase transition occuring in P2-$Na_{0.67}Mn_{0.75}Ni_{0.25}O_2$, in order to avoid fast capacity decay. One successful strategy for suppressing this phase transition is metal-ion doping.[12] So far, several doping elements have been reported in literature, such as Fe, Cu, Co and Mg.[16,17–19] Depending on the doping element, the electrochemistry might be slightly different, e.g. Fe also participates in the electrochemistry. Dopants like the Mg^{2+} cation are electrochemically inactive and, when occupying a TM site, they are expected to increase the high potential stability by suppressing the P2-O2 transition. The aim of the doping is to subdue the unstable O2 phase by forming the so-called OP4 phase, described as an arrangement of alternating layers of P2 and O2.[20] However, the mechanism of the formation of the OP4 phase is hardly understood for Mg-doped Mn-Ni oxides. We found that Mg doped layered P2-MnNi oxides do not undergo a two-phase reaction from P2 to the OP4 phase but form many different intermediate structures similarly to a layered P2-NaFeMn oxide.[21,22] We also illustrate the challenges in refinement, identification and characterization of the new phases by comparing simulated OP4 and O2 structures with operando synchrotron studies to understand

the structural changes. The results are complemented by an investigation of the phase stability of the O2, P2 and OP4 phases with respect to the degree of Mg doping employing periodic DFT calculations.

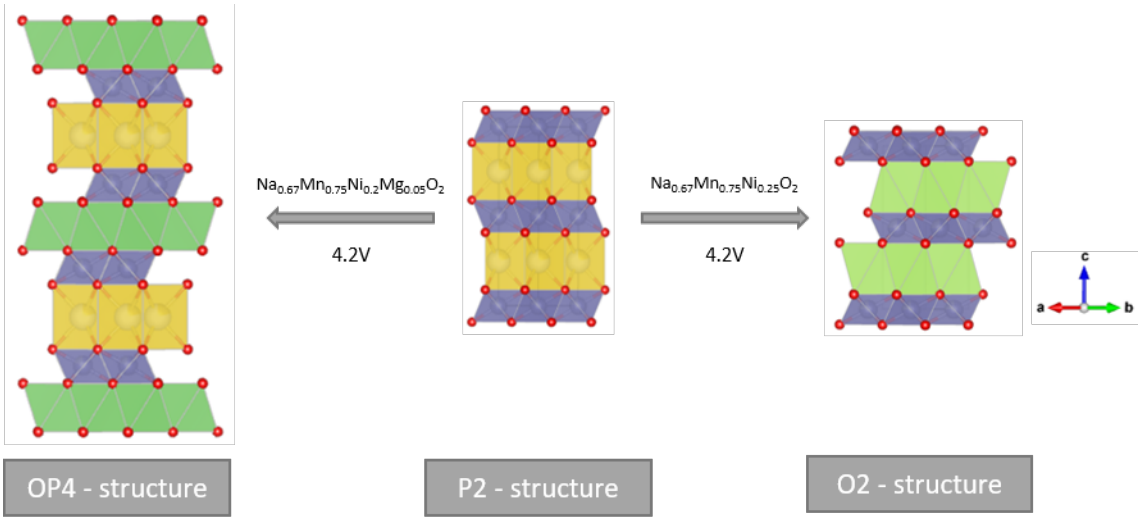

Figure 1: Schematic figure of the OP4 structure (green: empty Na position, yellow: occupied Na position, purple: Mg, Ni and Mn position), the P2 structure (yellow: occupied Na position, purple: Mg, Ni and Mn position) and the O2 structure (yellow: empty Na position, purple: Ni and Mn position).

EXPERIMENTAL SECTION

Material synthesis

P2-$Na_{0.67}Mn_{0.75}Ni_{0.25}O_2$ (P2-MNO) and P2-$Na_{0.67}Mn_{0.75}Ni_{0.20}Mg_{0.05}O_2$ (P2-MNMO) were synthesized via a 2-step synthesis. A $Mn_{0.75}Ni_{0.25}(OH)_2$ precursor was synthesized via co-precipitation in a continuous stirred tank reactor (CSTR, V = 1L), by mixing $Ni(NO_3)_2$*4 H_2O, $Mn(NO_3)_2$*6 H_2O, NaOH and NH_3 solution (Carl Roth) in appropriate ratios. The preparation procedure is described by Pfeiffer et al. in more detail.[23] Afterwards the precursor was dried and sieved in order to obtain homogenously sized particles. In the following step, the P2-MNO precursor was mixed by wet impregnation with an aqueous NaOH solution (7 mol/L), while the P2-MNMO precursor was mixed by wet impregnation with 3.7 wt% $MgCO_3$ and with a (7 mol/L) aqueous NaOH solution in appropriate ratios. The mixture was then dried at 140°C for 3 hours and the obtained powder was ground and calcinated at 900°C in a Nabertherm batch furnace for 12 hours under air atmosphere, followed by a passive cooling step to 200 °C. The powder was immediately transferred into a Büchi Glass oven and it was kept under vacuum ($<3\cdot10^{-5}$ hPa) at 200°C overnight. In the following the dried powder was transferred and stored in an Argon (Ar) filled Glovebox (MBraun H_2O < 0.1 ppm, O_2 < 0.1 ppm).

Material Characterization

Powder X-ray diffraction (PXRD) patterns were recorded in Bragg-Bretano geometry in the 2θ range 10–90° with a step size of 0.01° on a D8Advance (Bruker) diffractometer using $Cu_{K\alpha1}$ X-ray tube (λ = 1.54051 Å) and a LynxeyeXE detector. The PXRD data analysis was carried out via Rietveld Refinement by using the Topas V6 software. Chemical analyses were performed by inductively coupled plasma optical emission spectroscopy (ICP-OES) measurements (Spectro Arcos SOP). The sample morphology was analysed by scanning electron microscopy (SEM), using a Leo Gemini 1530 VP instrument, images were generated at accelerating voltage of 5 kV with an Everhart-Thornley-SE-Detector. Scanning transmission electron microscopy (STEM) was carried out to determine the local crystal structure and elemental composition. A Thermofisher Talos 200X (S) TEM operated at 200 kV was used. The system was equipped with a dedicated SuperX energy dispersive X-ray detector (EDX)

for spectroscopy and elemental maps. The samples were drop-casted on holey carbon films prior to the STEM investigation.

Operando synchrotron diffraction (SXRD) was performed at the Material Science and Powder Diffraction beamline (MSPD) at the ALBA facility (Barcelona) by using a source radiation with λ = 0.4132 Å wavelength (30 keV) and the MYTHEN position-sensitive detector. Data was gathered in steps of 0.006° over an angular range of 1.8–42° (2θ geometry) with an effective exposure time of 60 s per pattern. The cells were cycled at C/10 rate (1C = 173 mA/g). The coin cells were continuously oscillated +/-5° around the incoming beam direction to improve powder averaging (e.g. increasing the number of crystallites contributing). The electrochemical cells, used for the *operando* synchrotron measurements, consisted of 2032-type coin cell with a 5 mm diameter circular glass window for the beam entrance. For both *operando* techniques, the positive electrodes had a mass loading of ~10 mg*cm^{-2} with a composition of 84 wt.% Active Material, 8 wt.% Carbon Black, and 8 wt.% PVDF. Metallic sodium was used as a counter electrode with a 5 mm center hole (only for synchrotron), 150 µL 1 M sodium hexafluorophosphate ($NaPF_6$) in propylene carbonate (PC) + 5% fluoroethylene carbonate (FEC) served as electrolyte solution, and Whatman GF/A served as separator.

The FullProf software package was also used to plot simulated XRD-patterns of O2-$LiCoO_2$ and of OP4-$(LiNa)_xCoO_2$ structures. [24]

Electrode preparation and electrochemical testing

Electrode slurry preparation and coating were performed inside an Ar-filled Glovebox (Mbraun ®). The as-synthesized active materials P2-MNO and P2-MNMO were dry mixed with mortar and pestel together with PVDF as a Binder and Super P conductive carbon in a 84:8:8 ratio. Afterwards the slurries were prepared by adding NMP (N-methyl-2-pyrrolidone) under constant magnetic stirring for 3 hours at 300 rpm. The slurry was cast onto an Al foil current collector, with mass loading of ~4-5 mg·cm^{-2}. The coated foil was dried at 80 °C for 1 h and at RT overnight. Circular 12mm diameter electrodes were punched and dried overnight at 130 °C under dynamic vacuum in a Büchi glass oven. Galvanostatic cycling experiments were performed in 3 electrode T-cells, with a VMP3 (BioLogic) multichannel potentiostat. Metallic sodium was used as counter and quasi-reference electrode. Circular Whatman GF/A glass fiber was used as separator. A 1 M $NaPF_6$ (99.99% Sigma-Aldrich) in PC + 5% FEC solution

was used as electrolyte. Electrochemical cells were charged/discharged at different current rates in the 2.00 V- 4.30 V (vs. Na/Na^+) range. Galvanostatic Intermittent Titration Technique (GITT) measurements were carried out with a current pulse at C/100 rate (~24 μA) applied for 1 h, followed by a relaxation until the potential change was below 5mV h^{-1}.

Computational Details

Spin-polarized periodic density functional theory (DFT) [25] calculations were performed to investigate the phase stability of the P2, O2 and OP4-structure type in $Na_xMn_{0.75}Ni_{0.25-y}Mg_yO_2$. Exchange and correlation were accounted for by using the Perdew-Burke-Enzerhof (PBE) functional and the Grimme D3 correction was applied to capture dispersion effects.[26] The Projector Augmented Wave (PAW) method was employed to represent the electron-core interactions as implemented in Vienna *Ab initio* Simulation Package (VASP).[27] To account for the highly localized nature of the *d*-electrons in the 3*d*-metals Mn and Ni a Hubbard-like *U* correction was applied using the *U* parameters U_{Mn} = 3.9 eV and U_{Ni} = 6.2 eV.[28] Calculations were performed for the P2, O2, and OP4 structures for varying Na concentrations using a supercell containing 24 and 32 formula units in the case of the P2 and O2 structure and 48 and 64 formula units in the case of the OP4 structure, respectively (see Figure S5 in the Suppl. Materials). All calculations were performed with a plane wave cutoff of 520 eV and the Brillouin zone was sampled using a 3x3x3 k-point mesh for the O2 and the P2 structure and a 3x3x2 k-point mesh for the OP4 structure accounting for the larger c parameter of the OP4 supercell. The electronic convergence criterion was set to $1x10^{-6}$ eV and the experimental atomic positions and lattice constants were used and relaxed without any restriction until the forces on the atoms were converged below 0.01 eV $Å^{-1}$.

Discussion

Material characterization

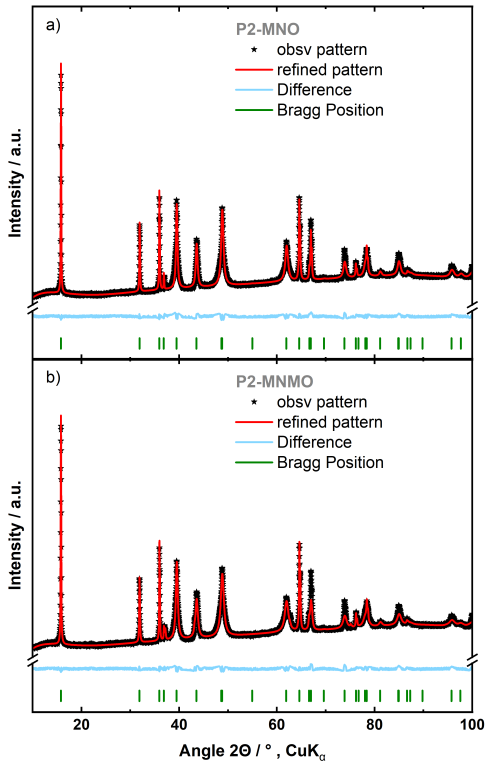

Figure 2: a) refined PXRD of P2-MNO; b) refined PXRD of P2-MNMO with 1.31 % MgO/NiO impurities.

Phase pure P2-MNO was prepared as baseline material, and compared to the P2-MNMO. The following section presents a detailed physical and electrochemical characterization of P2-MNMO. The materials chemical composition was determined by ICP-OES, yielding in $Na_{0.61}Mn_{0.75}Ni_{0.25}O_2$ and $Na_{0.62}Mn_{0.75}Ni_{0.21}Mg_{0.04}O_2$ for the P2-MNO and for P2-MNMO phase, respectively. **Fehler! Verweisquelle konnte nicht gefunden werden.**a/b shows the Rietveld refinement from PXRD data of P2-MNO and P2-MNMO. Both materials could be indexed as a P2-type structure (space group *P*63/*mmc)*. By having a closer look at the patterns for both P2-MNO and P2-MNMO, the (10*l*) ((102), (104), (106) and (108)) reflections show peak broadening, which point out the possible presence of stacking faults as shown in our previous publication.[23] The determination of the successful incorporation of Mg into the crystal structure respectively into the TM sites is quite challenging, since Mg (0.72 Å) and Ni (0.69 Å) have very similar ionic radii. Based on Rietveld refinement results (shown

in **Fehler! Verweisquelle konnte nicht gefunden werden.**), the observed slight increase in cell volume might indicate an enlargement of the lattice due to the larger Mg^{2+} ion. Characteristic reflections of MgO and NiO have been found for P2-MNMO, which is expected since the precursor already has a fixed Mn:Ni stoichiometry ratio of 3:1. Even though the precursor has a fixed stoichiometry and an ion exchange between Mg and Ni is forced, it is mainly used due to its spherical particle shape leading to spherical shaped P2-MNO and P2-MNMO particles (Figure 3a, b).

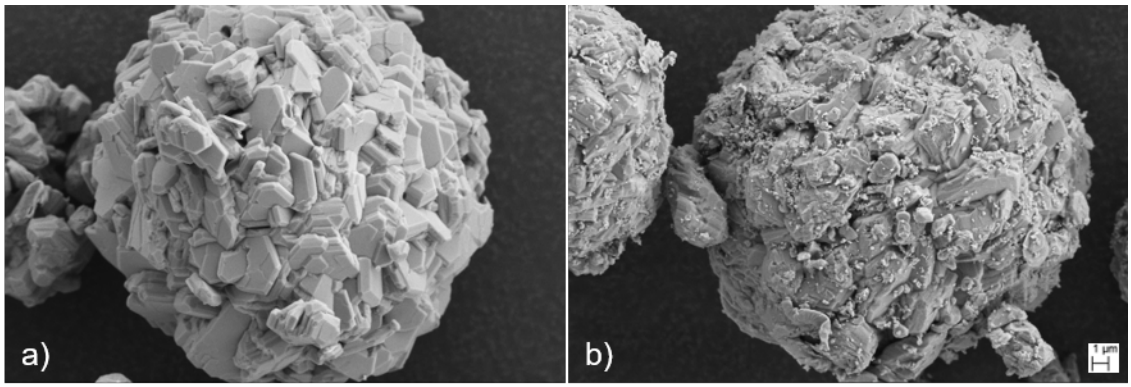

Figure 3: a) SEM image of P2-MNO shows spherical polycrystalline particle b) SEM images of P2-MNMO shows spherical polycrystalline particle with small Nanocrystalites on the surface.

Spherical shaped particles tend to show good tap density, thus being able to allow the development of high density (and high energy) electrodes.[29] Moreover, spherical powders are known to have better processability, which may be beneficial to the manufacturing process of high-quality electrodes.[30] Besides the spherical morphology, the hydroxide-based co-precipitation method is scalable and allows for the design of cathode materials possessing good homogeneity and well-defined chemical composition.[31]

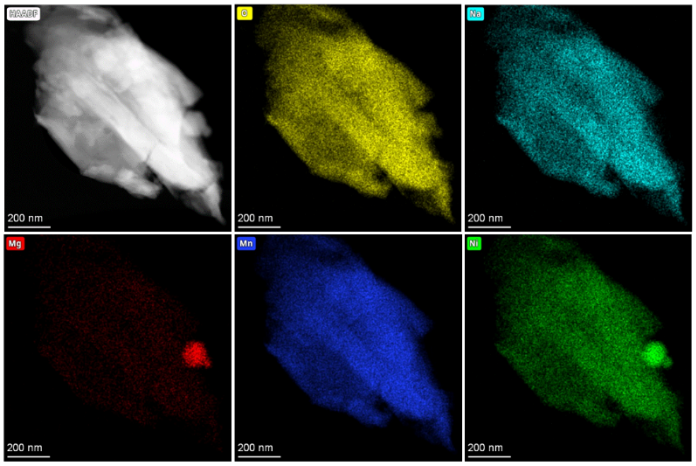

Figure 4: (top left) STEM high angle annular dark-field images (HAADF) and corresponding EDX mappings of a cracked P2-MNMO particle. The mappings illustrate the distribution of O (yellow), Na (turpuoise), Mg (red), Mn (blue), Ni (green) of P2-MNMO.

In order to further underline the statement of a successful, and more importantly, homogeneous doping of Mg^{2+} into the transition metal sites, local STEM investigations, and the acquisition of energy dispersive spectroscopy (EDS) maps of cracked P2-MNMO particles were performed. The elemental distribution of the STEM data in Figure 4 shows that Na, Mn, Ni, Mg and O are uniformly distributed, except for the occurrence of some local Ni/Mg clusters most likely associated with MgO/NiO impurities.

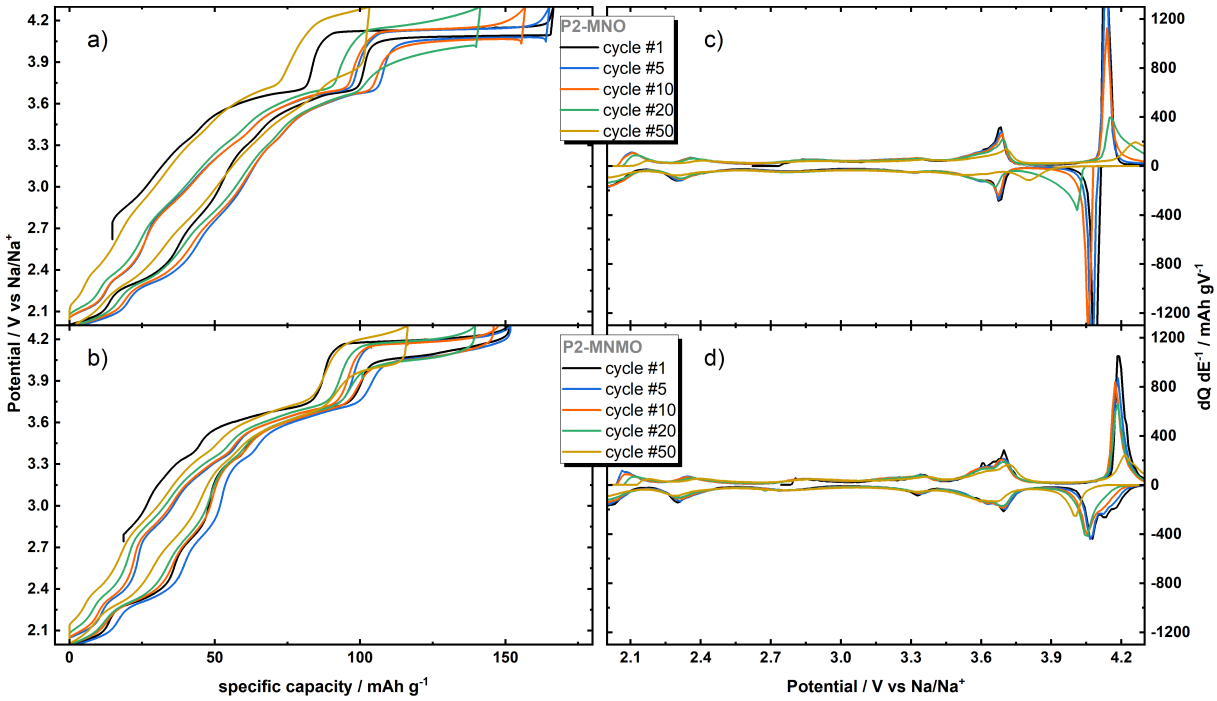

Figure 5: a)/b) electrochemical profile of selected cycles of P2-NMO/P2-MNMO c)/d) corresponding differential analysis of P2-NMO/P2-MNMO.

Electrochemical performance was investigated by comparing P2-MNO and P2-MNMO in the potential range of 2.00 V< E (V Vs. Na/Na^+) < 4.30 V. Specific capacity for cycle 1 and cycle 2 charge was 151 $mAhg^{-1}$ and 173 $mAhg^{-1}$ for P2-MNO and 133 mAhg-1 and 156 mAhg-1 for P2-MNMO, respectively. Charge- discharge profiles of a 0.1 C (1 C = 173 mA/g) current rate galvanostatic experiment, are shown in **Fehler! Verweisquelle konnte nicht gefunden werden.**a,b. The reason for the lower 1st charge capacity of P2-MNMO can be easily explained by considering that Mg, as opposed to Ni, is electrochemically inactive. As reported on similar materials, the electrochemical profiles in the region of E = 2.00 V - 4.00 V (vs. Na/Na^+) are smooth and sloping for both samples, indicating a solid solution

reaction mechanism.[17] It clearly confirms that by changing the stoichiometric Mn:Ni ratio from 2:1 to 3:1, the honeycomb transition metal ordering within the transition metal slab is weakened.[6] By having a closer look into insertion and extraction processes (**Fehler! Verweisquelle konnte nicht gefunden werden.**c, d), the biggest contribution to specific capacity is attributed to Ni activity: Reversible peak couples in the E = 3.00 V - 3.90 V (vs. Na/Na^+) potential region can be attributed to the redox reactions of Ni^{2+}/Ni^{3+} and Ni^{3+}/Ni^{4+}.[32] Smaller peaks, located in the E= 2.00 V - 2.80 V (vs. Na/Na^+) region are attributed to the redox activity of the Mn^{3+}/Mn^{4+} couple.[33]

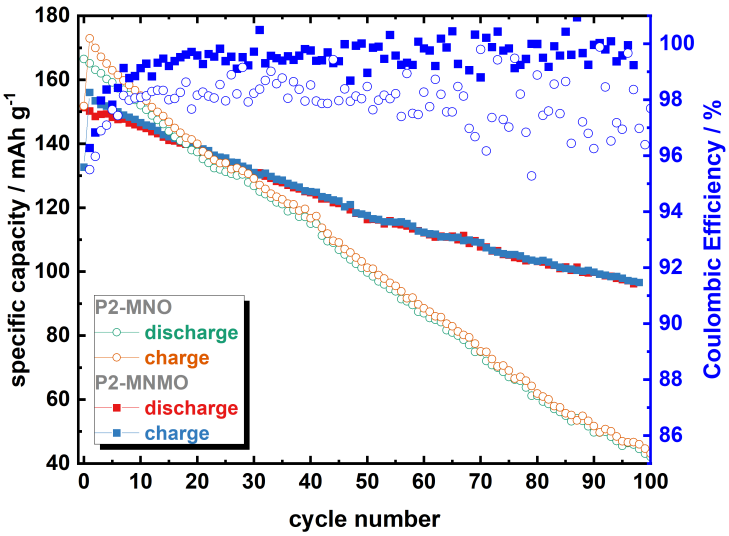

Figure 6: Charge and discharge capacity for 100 cycles of NMO and MNMO with the corresponding Coulombic Efficiency.

The hysteresis in oxidation and reduction potentials for both materials in the 2.00 V - 4.00 V (vs. Na/Na^+) potential range is low, which indicates good kinetics and low polarisation. As expected, the main difference between the electrochemical behaviour of the two materials is visible in the higher potential region, E= 4.00 V - 4.30 V (vs. Na/Na^+), where the P2-O2 phase transition is expected to occur.[6] For the first cycle in P2-MNO, the plateau at E= ~ 4.10 (vs. Na/Na^+) is well defined, whereas for P2-MNMO, the plateau during the first cycle shows a sloping character. Furthermore, by comparing P2-MNO and P2-MNMO redox peaks couples (Figure 5 c-d), the shapes seem to be different, which indicate the presence of a different phase transition. The increased cycling stability points to the doping induced formation of a new phase.[17,34] During the first couple of cycles, the P2-MNO seems to be advantageous since it shows high initial capacities with rather low hysteresis at the high potential plateau. However, after 10 cycles the hysteresis of P2-MNO strongly increases while for P2-MNMO, it

starts to slightly increase after cycle 40. By comparing the galvanostatic profiles at different cycle numbers, the decrease in specific capacity is clearly located in the high potential region for both P2-MNO and P2-MNMO materials. However, the P2-MNO capacity decreases much faster and, as illustrated in Figure 6, reaches 140 mAh g^{-1} already at cycle 20. This behaviour is also reflected in capacity retention values at cycle 100, which were 25.5 % for P2-MNO (156 mAh g^{-1} to 45 mAh g^{-1}) and 64.0% for P2-MNMO (133 mAh g^{-1} to 96 mAh g^{-1}), respectively.

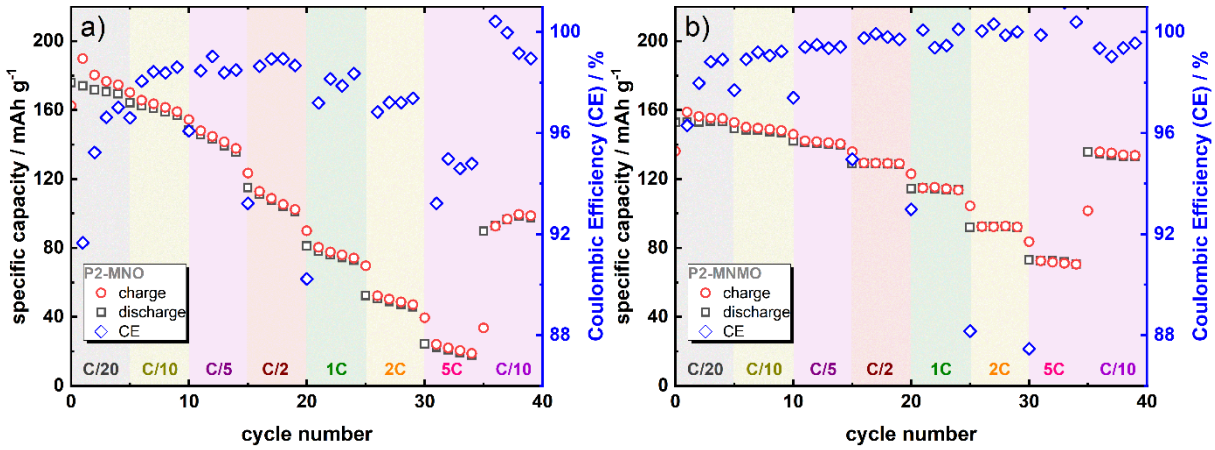

Figure 7: Rate performance of P2-NMO (a) and P2-MNMO (b) at various current rates ranging from C/20 to 5C.

Rate performance of both P2-MNO and P2-MNMO was evaluated in the voltage range of 2.00 V - 4.30 V (vs. Na/Na^{+}), as presented inFigure 7a/b. Reversible specific capacities progressively decrease from 170 mAh g^{-1} at C/20 to 34 mAh g^{-1} at 5C for P2-MNO and 159 mAh g^{-1} to 72 mAh g^{-1} for P2-MNMO. (Table S3). On the one hand, it is clear that the baseline P2-MNO cathode material experiences a higher polarization with increasing current rate, thus achieving remarkably lower specific capacity and coulombic efficiencies. On the other hand, P2-MNMO shows a much more regular cycling behaviour, higher coulombic efficiencies and, in general, higher specific capacities, with the exception of the C/20 rate. Capacity recovery during the final C/10 current rate step, is better for the P2-MNMO, indicating less pronounced aging during the rate capability test for P2-MNMO.

To further show the effect of Mg^{2+} doping, the apparent Na^+-diffusion coefficient has been investigated by using Galvanostatic Intermittent Titration Technique (GITT).[35]

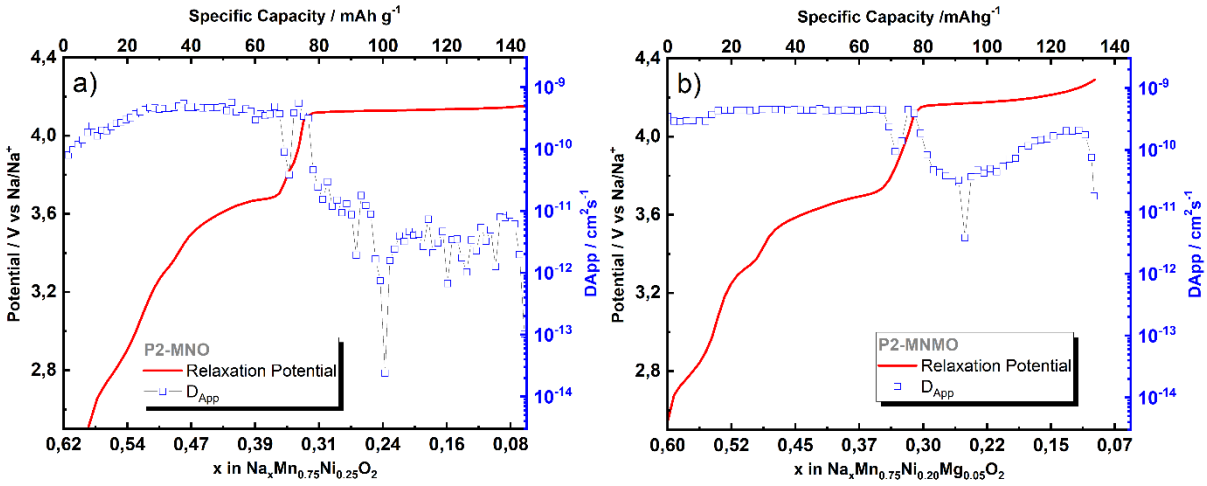

Figure 8: Apparent Na^+ diffusion coefficient (D_{App}) calculated from GITT (C/100 current pulse – 1h) measurements for (a) P2-MNO and (b) P2-MNMO as a function of the potential.

It is known that GITT is more reliable for measuring the chemical diffusion coefficient than other techniques, like Potentiostatic Intermittent Titration Technique (PITT) based on more efficient elimination of parasitic background current distribution.[36] However, electroanalytical methods like GITT, PITT or cyclic voltammetry (CV) are based on the assumption of one-dimensional diffusion in a solid solution electrode and do not consider phenomena like phase transformations.[37] Using conventional electroanalytical methods result therefore only in an apparent diffusion coefficient. In this case, the sodium ion apparent diffusion coefficient can be obtained by the following expression, derived from the 2nd Fick's law:

$$D_{Na^+} = \frac{4}{\pi}\left(\frac{m_B V_M}{M_B S}\right)^2 \left[\frac{\Delta Es}{\Delta E_t}\right]^2 (t \ll L^2/D),$$ with m_B=mass of component B, M_B atomic weight of B, S=area of the sample-electrolyte interface, ΔE_s=change of equilibrium voltage, ΔE_t= change of cell Voltage E during the current pulse, neglecting the IR drop.

Fehler! Verweisquelle konnte nicht gefunden werden. presents the apparent chemical diffusion coefficient of the charge of Na-ions (D_{Na}^+) for P2-MNO in comparison with P2-MNMO determined from the GITT profiles (**Fehler! Verweisquelle konnte nicht gefunden werden.**). For both materials in the solid solution region, with a Na content between $0.6 < x < 0.3$ ($x = Na^+$), the D_{Na+} apparent

diffusion coefficients are comparable. The diffusion coefficient values are in between 10^{-9} and 10^{-10} cm^2 s^{-1}.

By having a closer look at the reported plot (Figure 8), P2-MNMO shows more stable diffusion coefficients, with less fluctuations. Instead, when the upper potential region (E= 4.10 V (vs. Na/Na^+)) is reached, with a sodium content of x = 0.3, respectively the P2-O2 phase transition occurs in P2-MNO and the diffusion coefficient decreases to values in the range of 10^{-11} cm^2 s^{-1} and 10^{-13} cm^2 s^{-1}. The behaviour for the Mg^{2+} doped P2-MNMO seems to be quite different, in fact D_{Na+} values initially decrease to similar values, close to 10^{-11} cm^2 s^{-1}, while a successive increase to 10^{-10} cm^2 s^{-1} at the end of charge is observed. For the P2-MNMO material, the fluctuation of the calculated diffusion coefficients at the end of charge is low. This observation underlines faster kinetics during the phase transition for the Mg^{2+} doped sample, which is in good agreement with a report by Singh et al.[3]

In order to understand more about the phase transition occurring in the Mg doped sample a detailed analysis is required. In literature reports about Na-Mn-Ni-oxides, the term "OP4 structure" is used when Mg is inserted as dopant. The scarce available literature describes the occurrence of the OP4 structure as a shoulder of the 002 reflection from the P2 phase by means of operando measurements.[17,19]

Both OP4 and O2 structures were initially investigated in layered Li-ion cathode materials.[38,39] Berthelot et al. reinvestigated the properties of $(LiNa)_xCoO_2$ and assigned it to an OP4 structure with alternating octahedral coordinated Li and trigonal-prismatic coordinated Na_e/Na_f layers which can be, unlike OP4-$Na_xMn_{0.75}Ni_{0.2}Mg_{0.05}O_2$, synthesized.[40] The origin of the O2 structure results from an O2-$LiCoO_2$ which is also synthesizable in contrast to O2-$Na_xMn_{0.75}Ni_{0.25}O_2$.[39] Interestingly, the Li-based O2/OP4 models (figure S3), that are described in literature are a good starting point for gaining first insights in the structure evolution of these cathode materials. However, to allow for a more realistic interpretation of the observed operando diffraction data, PXRD patterns were derived from DFT optimized $Na_0Mn_{0.75}Ni_{0.25}O_2$ an $Na_{0.17}Mn_{0.75}Ni_{0.17}Mg_{0.08}O_2$ structure models.

VESTA software was used to simulate PXRD patterns for the O2 and OP4 structures resulting from the periodic DFT calculations of $Na_0Mn_{3/4}Ni_{1/4}O_2$ and of $Na_{0.17}Mn_{0.75}Ni_{0.17}Mg_{0.08}O_2$ described in the computational section.[41] The structures obtained by DFT offer the advantage that the lattice constants

are optimized for the Na containing compounds. The Bragg peak intensities were calculated within VESTA and the resulting patterns (see Figure S1) will be used for direct comparison with the *operando* data discussed below.

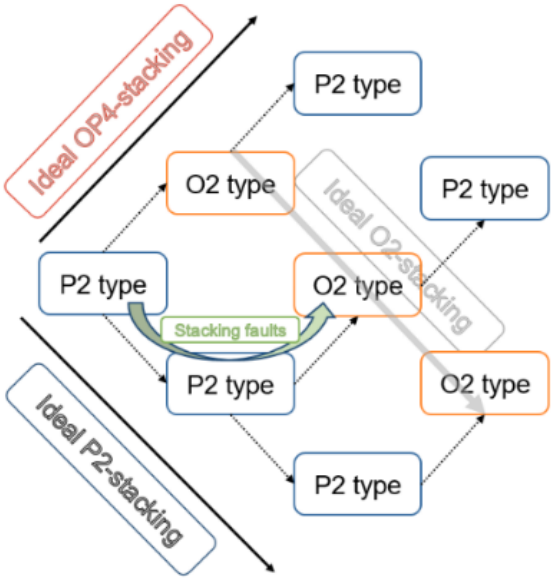

Figure 9: Schematic figure of the formation of P2, O2 and OP4 structure.

Additionally, it should be also expected that the replacement of Ni with Mg might not occur completely homogeneously, which is dependent on the amount of the doping agent. In case of an inhomogeneous Mg distribution into the TM Layers, stacking faults will occur, which could influence the alternating layer arrangement of P2 and O2 phases as schematically described in Figure 9.

For a more detailed investigation of the crystal structure of the high potential phase, *operando* XRD studies for the sodium (de-)intercalation have been carried out for P2-MNO and P2-MNMO. Contour Maps of selected areas during the first charge and discharge are shown in **Fehler! Verweisquelle konnte nicht gefunden werden.**. Detailed diffraction patterns in combination with the electrochemical profile (2 electrode setup – cell voltage denoted as U) are shown in **Fehler! Verweisquelle konnte nicht gefunden werden.** for P2-MNO and in **Fehler! Verweisquelle konnte nicht gefunden werden.** for P2-MNMO.

At the initial stage of the charging process for P2-MNO, all reflections can be assigned to the typical P2-type structure with a space group of *P*63/*mmc.* At the beginning of the first charge for P2-MNO, in

the 2.00 V < U(V) < 4.00 V range, (002) and (004) reflections gradually shift to lower angles while (100), (110) and (112) reflections shift to a higher angle, suggesting a solid solution reaction mechanism. The gradual shift of the 00*l* planes to lower diffraction angles indicates an expansion of the c-parameter, while the shift to lower angles for (100), (10*l*) and (11*l*) indicate a contraction of the a parameter.[39]

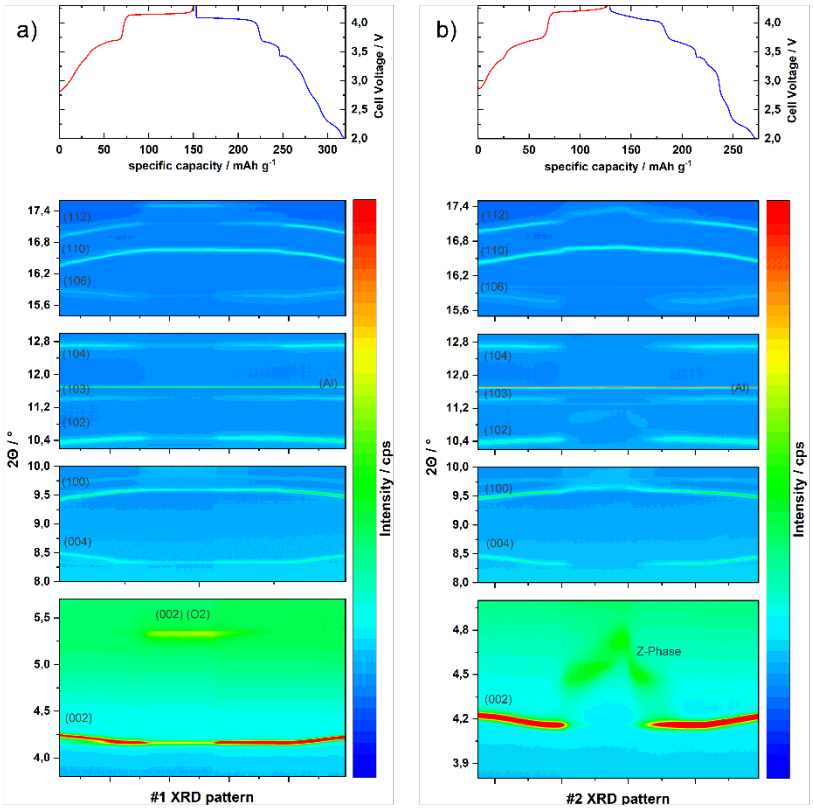

Figure 10: Contour Maps of operando synchrotron XRD measureemnt of a) P2-MNO and b) P2-MNMO.

When charging to U= 4.200 V the (00*l*) reflections remain at constant position and progressively decrease in intensity. At the same time, new reflections appear at 5.35°, 9.95° and 17.50° 2Θ, suggesting a 2-phase region. Comparing the experimentally observed diffractogram with the simulated diffraction pattern based on DFT calculations (Figure S5) shows that the (002) reflection at 5.26° 2Θ (DFT-based) of the O2 structure agrees well with the experimentally measured reflection (5.35° 2Θ). Moreover, reflections with relatively high intensity in the region of 9°-10° 2Θ and 17°-18° 2Θ are expected based on simulated diffraction patterns, but cannot be unabmigously assigned to the experimentally observed reflections.

Since multiple factors like the large carbon background, very low intensity and possible P2/O2-reflections overlapping come into play, a clear assignment to the refinement of this phase is rather difficult.

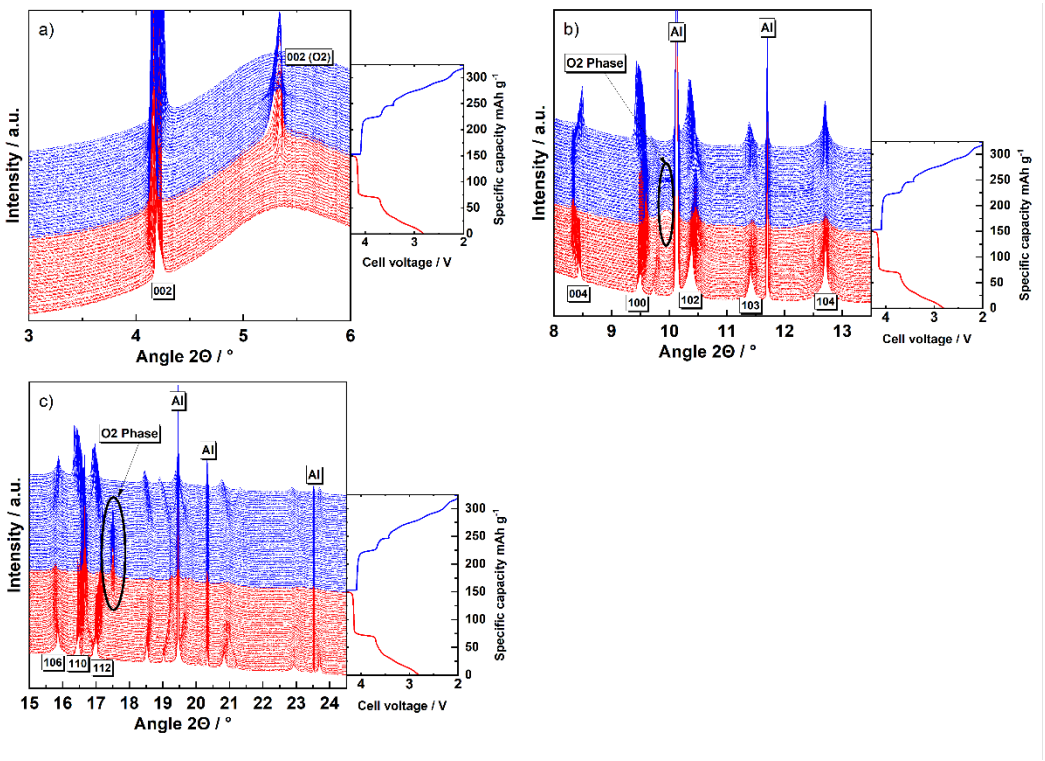

Figure 11: *Operando* synchrotron XRD of P2-MNO in the region of 3-6° 2Θ, illustrating the phase evolution during charge and discharge.

However, we already reported an additional O2-phase reflections apart from the (002) hkl plane.[38] The (004) hkl plane at around ~38° 2Θ (using a Cu X-ray tube) was identified, which is in close range to the observed reflection at 9.95°, when using a radiation source of λ = 0.4132 Å. At the end of charge, at E= 4.300 V (vs. Na/Na^+), P2 reflections are still present with a significant intensity, indicating that the P2→O2 phase transition is not complete. This observation is consistent with possibly slow kinetics of the material. Another possible explanation could be the instability of the O2 phase, which has been proved with electrochemical measurements.[6] In addition, when looking at the second cycle charge step of the *operando* XRD experiment, presented in **Fehler! Verweisquelle konnte nicht gefunden werden.**, the reflections show decreased intensities, and lower range of (002) O2 reflections, which match the shorter plateau to the capacity loss due to the phase transition.

Operando XRD measurements carried out with P2-MNMO (**Fehler! Verweisquelle konnte nicht gefunden werden.**), show the typical P2-type structure with a space group of *P*63/*mmc.* Additional reflections, which could be indexed to MgO and/or NiO, have been observed as well.

In the 2.00 < U(V) < 4.00 region, P2-MNMO shows a solid solution behaviour similar to P2-MNO.[39] However, upon further charging, all reflections assigned to the P2-phase start to decrease in intensity until they almost completely disappear. This behaviour indicate an almost complete phase transition. As the P2-structure related reflections start to decrease, new, small and broad reflections appear at 4.46°, 9.6°, 10.8°, 16.6° and 17.2° 2Θ. To the best of our knowledge so far, in literature for Mg-doped sodium-manganese-nickel-layered oxides, only the reflection at around 4° - 5° 2Θ has been reported.[17,18] This reflection was either assigned to the 'OP4' phase or reported as a shoulder of the $(002)_{P2}$ reflection.

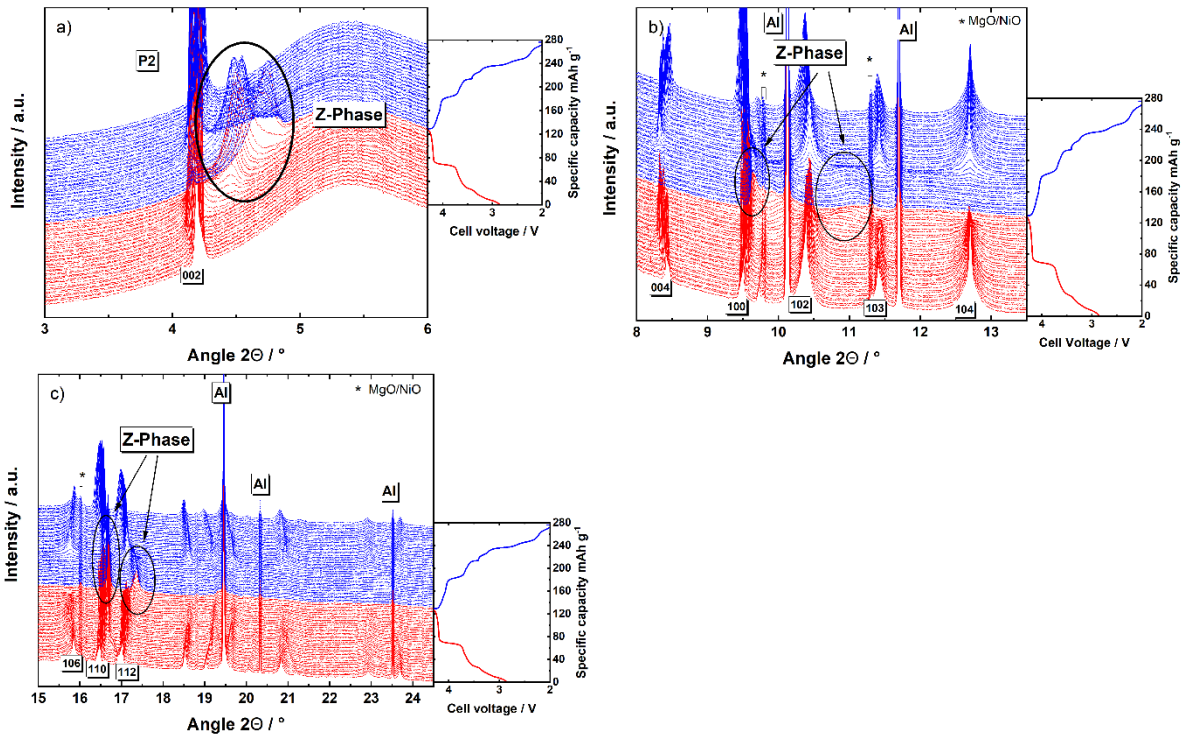

Figure 12: O*perando* synchrotron XRD of P2-MNMO in the region of 3-6° 2Θ, illustrating the phase evolution during charge and discharge.

Surprisingly, this reflection became broader and shifted to higher angles upon further charging to U= 4.30 V. The continuous shift to higher angles could be a consequence of the increasing amount of O-type layers, which means that there is possibly not only one specific 'OP4' structure but many intermediate structures like it has been already reported for $Na_{2/3}[Ni_{1/6}Mn_{1/2}Fe_{1/3}]O_2$.[22] Additionally, the

huge broadening of this reflection could be an indication that these intermediate structures may exist at the same time. When comparing the reflection at the end of charge (4.73° 2Θ) with the calculated pattern obtained from the DFT geometry relaxation in Figure S5 (4.66° 2Θ), the observed interlayer distance matches with the interlayer distance of the structure obtained by DFT calculations. This could mean that, the so-called 'OP4' structure exists as an intermediate structure itself. However, overall, the phase transition seems to be more like a continious process, a so-called Z-phase, as Somerville et al. described for a layered manganese iron oxide with the difference that the Fe doped material can result in an O2 structure since Fe is redox active.[22] Moreover, it is the first time that additional reflections (9.6°, 10.8°, 16.6° and 17.2° 2Θ) besides the typical reflection at 4.46° 2Θ are observed. With subsequent charging these reflections seem to shift to higher angles alongside with the reflection at 4.46°. By comparing these reflections with the simulated OP4-$(Li,Na)_x$MnNi oxide pattern and the calculated patterns based on structures derived from DFT, an unambiguous assignment can not be made with absolute certainty, since many reflections are (partially) overlapping.

After charging P2-MNO and P2-MNMO to U= 4.30 V, cells were discharged to U=2.00 V and *operando* XRD patterns were recorded. At the beginning of the discharge step, the P2-MNO follows a reversible process compared to the charge.

The reflections of P2-MNMO located at 5.35°, 10° and 17.5° 2Θ decrease in intensity and the P2 related reflections regain in intensity. From U= 4.00 V to U= 2.00 the (002), (004), (100), (110) and (112) reflections follow the opposite trend compared to the charging process.

Looking at the initial discharge of P2-MNMO, starting from U =4.30 V differences to the charge step can be detected. The (004) reflection starts to slightly decrease from 4.75° 2Θ and splits into 2 reflections, as demonstrated in **Fehler! Verweisquelle konnte nicht gefunden werden.**. With subsequent discharging, the reflections at higher angles (4.7°) of the splitted reflection start to decrease in intensity while the reflection at lower intensity (4.58°) increases in intensity. At U= 4.20 V these reflections start to broaden with another split (4.54° and 4.49°) in which the higher angle reflection decreases and only the lower angle reflections remain. At the same time, P2-structure related reflections start to increase in intensity.

When reaching a voltage of U= 4.15 V, the reflection at 4.47° assigned to the Z-phase starts to decrease in intensity while the reflections of the P2-phase further increase in intensity. From 4.0V onwards the discharge follows the same behaviour like the P2-MNO material, which means that the (002) and (004) reflections gradually shift to higher angles while the (100), (110) and (112) reflections shift to lower angles.

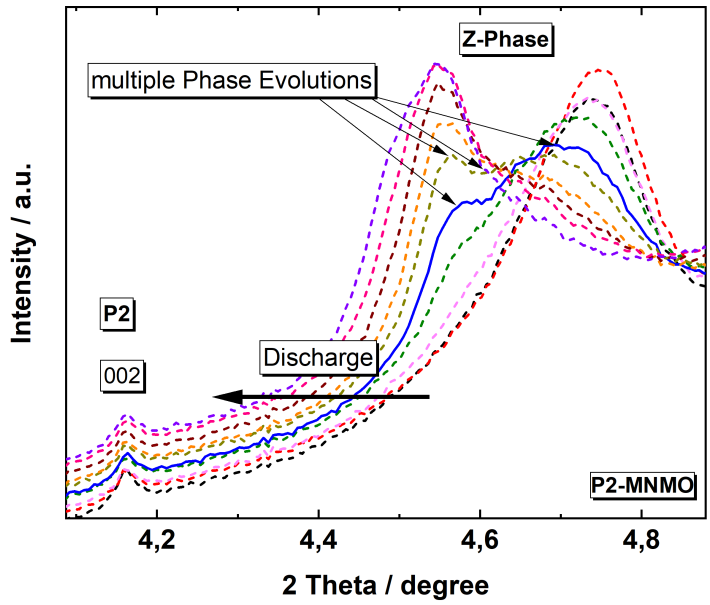

Figure 13: *Operando* synchrotron XRD of P2-MNMO during discharge at 4.3 - 4.2 V.

This asymmetric structural behaviour during charge and discharge is observed for Mg-doped Na-Mn/Ni oxides for the first time. While for Fe-doped Na-Mn/Ni oxides, the Z-phase seems to be comparable to Mg doped Na-Mn/Ni oxides during the charge, the discharge follows a different process. The Fe based Mn/Ni oxides show a reversible phase transition of this Z-phase, whereas the P2-MNMO show multiple reflection splits associated also in the multiple voltage plateaus during the discharge. In literature, it has been reported that the $O^{2-}/O_2^{(n-)}$ redox process for the layered P2-MNO materials leads to severe oxygen loss. Since Fe cations have a unique bonding interaction towards oxygen, the oxygen loss and therefore the fast degradation could be somehow prevented, which apparently also lead to a reversible charge/discharge profile.[42] Mg^{2+} on the other hand does not have the same unique behaviour of Fe cations since it cannot be oxidized but in general it has a strong ionic type interaction with oxygen, which could explain the differences during the discharge.

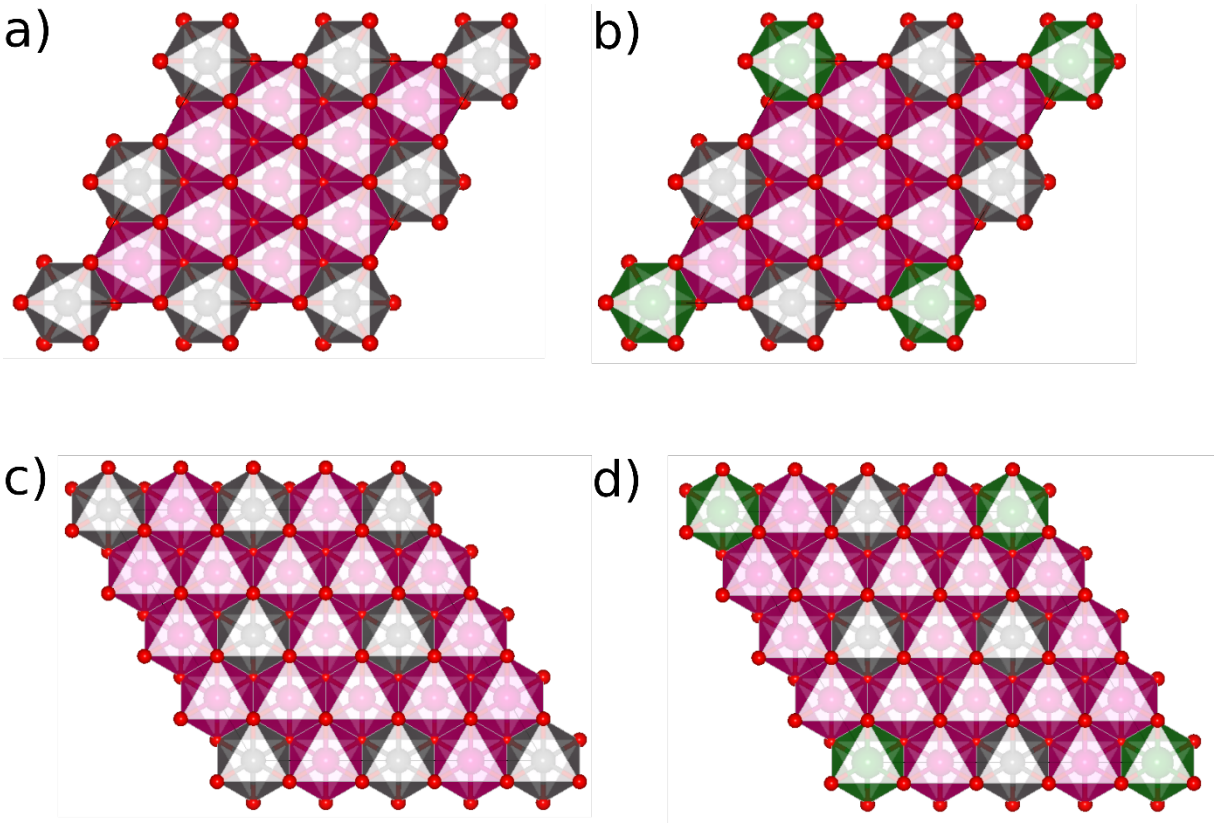

Figure 14: The supercells of the P2 structure used for the DFT calculations for the a) $Na_xMn_{0.75}Ni_{0.25}O_2$ compounds and the b) $Na_xMn_{0.75}Ni_{0.17}Mg_{0.08}O_2$ compounds exhibiting the defected honeycomb superstructure as well as the c) $Na_xMn_{0.75}Ni_{0.25}O_2$ compounds and the d) $Na_xMn_{0.75}Ni_{0.19}Mg_{0.06}O_2$ compounds exhibiting the TM order characterized by a maximized Ni-Ni-distance.

In order to understand the experimentally observed phase transformation behavior, we performed total energy calculations of various Na ion arrangements in the P2-, O2, and OP4-structure-types. In principle, a systematic evaluation of the phase stability would mean investigating all configurational degrees of freedom which might be achieved by employing cluster expansion methods including statistical sampling.[43] However, a systematic study of the three different phases O2, P2, and OP4 for various degrees of Mg doping and possibly various TM-orderings would require an immense computational effort. Instead, we chose to investigate the phase stabilities for particular model systems that were selected, based on experimental and theoretical findings and are described below. First, we probed various TM orderings to determine their respective stabilities for the P2 and O2 structure-type for the Na content x=0 without Mg doping. In the next step, we chose the two most stable TM orderings to calculate the phase stability of the three different phases O2, P2, and OP4 for various degrees of Mg doping. To account for the various possible Na arrangements at each Na content x we first determined

the stability of the various Na sites at low Na contents and then filled the structures by accounting for the optimal Na sites and the Na-Na repulsion as described in more detail below.

To start with, the considered configurations of the Mn, Ni, and Mg atoms within the TM layer are first described. To limit the computational effort, the stability of the TM configurations was solely investigated by considering two distinct TM arrangements. The first considered TM ordering – here referred to as "defected honeycomb" ordering - is based on previous experimental neutron powder diffraction (NPD) data suggesting an arrangement characterized by a $(\sqrt{3} \times \sqrt{3}) - R30°$ honeycomb superstructure corresponding to a network of edge-sharing $NiMn_6$ hexagonal units.[6,44] Therefore, the first supercell for our computational investigation (see Figure ***14*** a) and c)) was chosen to account for the reported formation of the $NiMn_6$ hexagonal units typical for the $Na_xMn_{2/3}Ni_{1/3}O_2$ compounds. At the same time, the employed Mn-Ni ratio in $Na_xMn_{0.75}Ni_{0.25-y}Mg_yO_2$ was accounted for by replacing one Ni atom per TM-layer at the center of a $NiMn_6$ hexagonal unit with a Mn atom, thus, introducing defects into the honeycomb structure. To represent the Mg-doped compounds additional Ni atoms were replaced by Mg according to the desired stoichiometry. Various possibilities to construct the described TM ordering were probed for the P2 structure and the O2 structure was consecutively constructed for the configuration showing the lowest energy.

The second considered TM ordering was achieved by maximizing the Ni-Ni distance in the TM sublattice to minimize the electrostatic repulsion within the TM layer. While the resulting TM ordering still contains $NiMn_6$ hexagonal units, these units are separated by additional Mn atoms to fulfill the required 3:1 ratio of Mn and Ni. Exemplary supercells based on this TM ordering are depicted in Figure ***14*** c) and d).

Both considered distinct TM orderings were found to be of very similar energy. While for the P2 structure the second ordering characterized by the optimized Ni-Ni distance shows a 5 meV lower energy the difference for the Na-free O2 structure was only found to be 1 meV.

Since both orderings have very similar energy, both were considered further. In the next step, phase stabilities of the P2, O2, and OP4 structure types for the two distinct TM orderings were calculated by considering a minimum of ten distinct Na ion arrangements per Na content and structure type. Since the

supercells for the considered TM orderings differ in size, the corresponding Na contents for the investigation of the phase stability also differ. While the supercell for the defected honeycomb arrangement contains 24 formula units, the supercell for the ordering for the optimized Ni-Ni distance contains 32 formula units. For the supercells with 32 formula units, highly ordered and stable structures were identified at a Na content of x=0.25, hence only the Na content range x=0-0.25 was chosen for the evaluation of the corresponding phase stabilities. In previous work, *Lee et al.* investigated the Na intercalation in the closely related $Na_xMn_{2/3}Ni_{1/3}O_2$ systems and showed that the Na ion arrangements strongly depend on both, the site energies as well as the in-plane Na-Na electrostatic repulsion.[45] Based on these findings we chose the Na ion configurations for the investigation of the phase stability for both considered TM arrangements by first determining the Na site energies for low Na contents, corresponding to one and two Na atoms per supercell, with respect to the distinct TM orderings and various degrees of Mg doping. In the O2-structure all Na sites are octahedrally coordinated by oxygen and our calculations for different arrangements indicate, that the most favorable Na sites for low Na contents share a face with the Ni or Mg polyhedrons. In the P2-structure the two prismatic edge-sharing Na_e and face-sharing Na_f sites are both prevalent in the structure (see Figure S5 (c) and (d) in the Suppl. Materials).[45] The Na_e sites are situated on the edges of the TM octahedra, while the Na_f sites share a face with the TM octahedron.[17,45] Our calculations of the Na site energies in the P2 structure for the $Na_xMn_{0.75}Ni_{0.25-y}Mg_yO_2$ compounds indicate, that the Na_e sites are the more stable sites, which may be due to a decreased Na-TM electrostatic repulsion, also being in agreement with literature [Lee, Signh].[17,45] The most stable Na_e sites in the P2 structure share an edge and a corner with a Ni or Mg octahedron in each neighboring TM layer to minimize the electrostatic Na-TM repulsion, thus, following the same trend as for the O2 structure. Interestingly, for the Mg-doped compounds, the Na_f sites sharing a face with a Mg and a Mn octahedron forming an Mg-Na-Mn dumbbell are only slightly less stable (4 meV for Mg content y=0.06 and 1meV for Mg content of y=0.08) than the most stable Na_e sites. The OP4-structure type is expected to form by complete deintercalation of the Na ions in every second layer of the P2-phase and subsequent gliding of the TM layers.[22] Therefore, the Na sites in the OP4-structure show a very similar coordination environment as the pure P2-structure type and exhibit the same observed trend. In the next step various Na arrangements for the maximal Na content x = 0.25 and x =

0.33 for the both TM arrangments were investigated by accounting for the maximal inter and intralayer Na-Na distance. The Na ion arrangements for the intermediate Na contents x = 0.13, x = 0.17, x = 0.19, and x = 0.25 were constructed employing these guidelines. Indeed, we have found that optimized Na-Na distances in combination with the lowest site energies lead to the most stable Na ion configurations for Na contents ranging from x=0-0.33. Previously, *Lee et al.* identified superstructures of the Na ion arrangement in the P2 structure-type for the Na contents x=0.33, x=0.5, and x=0.67 for the related $Na_xMn_{2/3}Ni_{1/3}O_2$ compounds and it was shown, that in the possible superstructure for the low Na content of x= 0.33 the Na ions are arranged in rows occupying Na_e sites.[45] Moreover, *Lee et al.* showed that the overall occupancy ratio of the Na_e and Na_f sites is determined by the competition between site energy and electrostatic repulsion. As described above the construction of the model system includes similar electrostatic arguments, indicating that the here chosen model system might indeed describe the Na ion arrangements for the Na content range x=0-0.33 sufficiently well to give a good estimate of the phase stabilities of the O2, P2, and OP4 structure types.

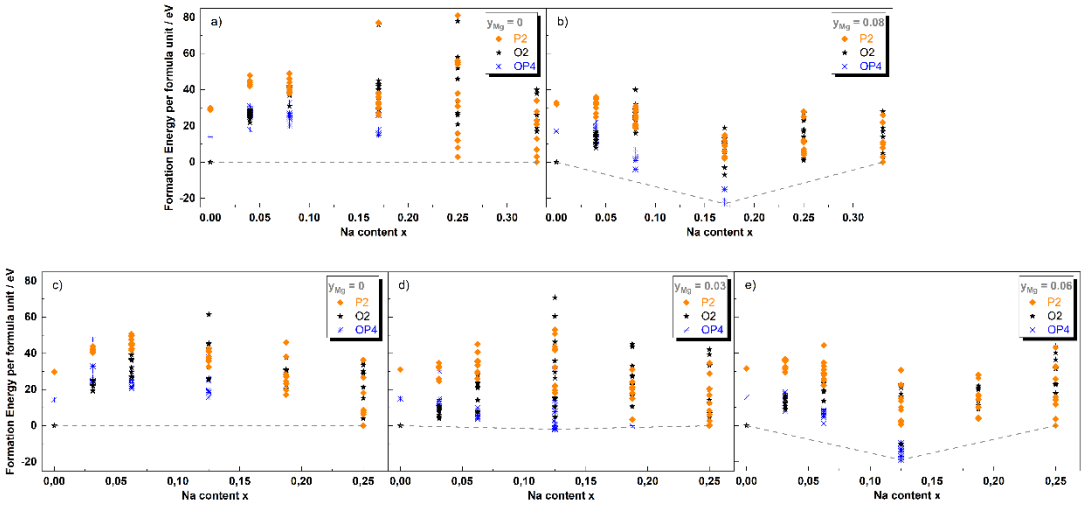

Figure 15: Formation energies per formula unit for the O2-, P2- and OP4-structure-type for various Na contents x for the a) undoped (y=0) and b) Mg-doped (y= 0.08) $Na_xMn_{0.75}Ni_{0.25-y}Mg_yO_2$ compounds exhibiting the defected honeycomb TM ordering. The energy hull relative to the phase separation into the respective empty O2- and the P2-phase with x = 0.33 is shown in black. Formation energies per formula unit for the O2-, P2- and OP4-structure-type for various Na contents x and the Mg contents y=0, y=0.03, and y= 0.06 for the $Na_xMn_{0.75}Ni_{0.25-y}Mg_yO_2$ compounds, containing the TM ordering with the optimized Ni-Ni distance. The energy hull relative to the phase separation into the respective empty O2- and the P2-phase with x = 0.25 is shown in black.

As for the energies of the Na sites, it was found that Na sites near Ni atoms are more energetically favorable than Na sites near Mn atoms. In addition, Na sites near Mg atoms were found to be the most stable sites. Which agrees well with the experimental finding of Mn oxidation taking place at low potentials (2-2.8 V) corresponding to high Na contents, while Ni oxidation occurs at high potentials (3-3.9 V), i.e., low Na contents (see **Figure *5***). Furthermore, this suggests that Na sites near the Ni atoms are likely to be energetically favorable due to the lower electrostatic repulsion between Na and Ni compared to Na and Mn. In addition, Mg is not redox active and is located at TM sites otherwise occupied by Ni. Therefore, Na sites near Mg are expected to be the most stable sites because the electrostatic repulsion between Na and Mg is the lowest. Thus, in agreement with the observed trend in Na site energies, the most stable sites are located near the Ni and Mg atoms.

The resulting energy-composition diagrams for the $Na_xMn_{0.75}Ni_{0.25}$-yMg_yO_2 compounds for the two distinct TM orderings are shown in Figure 15. The phase stabilities for the $Na_xMn_{0.75}Ni_{0.25-y}Mg_yO_2$ systems with Na contents ranging from x = 0-0.33 and the Mg doping contents of y = 0 and y = 0.08 obtained for the defected honeycomb TM ordering are shown in Figure 15 a)-b), while the phase stabilities for the $Na_xMn_{0.75}Ni_{0.25-y}Mg_yO_2$ compounds exhibiting the TM ordering with the optimized Ni-Ni distance with the Mg contents y=0, y=0.03, and y= 0.06 for the Na content range x=0-0.25 are shown in Figure 15 c)-e). The empty O2-structure (Na content x = 0) and the P2-phase with Na contents x = 0.33 or x=0.25 were chosen as reference phases for determining the formation energy per formula unit, respectively. In this framework, negative formation energies relative to the reference phases indicate phase stability with respect to the phase seperation into the reference phases, and the energy hull, indicated by the dotted line, needs to be adjusted to include all lowest energy structures. Independent of the TM ordering, the results for the Mg-free compounds indicate that phase separation into the empty O2-phase and the P2-phase with Na content x=0.25 and x=0.33 takes place in the whole concentration range x=0-0.25 and x=0-0.33. Increasing the Mg content gradually stabilizes the intermediate OP4 structure relative to the two reference phases resulting in a stabilization of the OP4-structure of about 20 meV per formula unit for the Mg content of y=0.08, as opposed to the formation of the O2 phase observed in the Mg free compounds.

As described in the experimental section, the Mg-free $Na_xMn_{0.75}Ni_{0.25}O_2$ compounds are observed to transform from the P2-phase at higher Na content to the O2-phase at low Na content, while the synthesized Mg-doped compound with y = 0.05 shows a transition from the P2-phase to the Z-phase, instead. Assuming that the formation of the Z-phase entails the formation of the OP4-phase allows to compare the phase stabilities obtained by the DFT calculations with the experimentally observed phases. Notably, the calculated phase stabilities of the OP4 structure follow a clear trend across the investigated TM orderings concerning the Mg content in the compound. This indicates that the Mg-doping stabilizes the OP4-phase at low Na contents, thus, explaining the experimentally observed formation of the Z-phase.

To allow for a more detailed comparison of the various results in this study, the evolution of the experimental d-spacing obtained from the SXRD measurements and the d-spacing obtained from the DFT results is depicted in Figure 16. The results labeled with the letter "-h" correspond to the defected honeycomb TM ordering, while the results labeled with the letter "-d" correspond to the alternative TM ordering characterized by the optimal Ni-Ni distance. The d-spacing is obtained for the (002) reflections in the case of the P2 and O2 structure and for the (004) reflection in the case of the OP4 structure. In general, the DFT results for both distinct TM ordering show very similar d-spacing comparing well with the experimentally determined ones. The results for the $Na_xMn_{0.75}Ni_{0.25}O_2$ compounds are shown in Figure 16 a) while the results for the Mg-doped $Na_xMn_{0.75}Ni_{0.25-y}Mg_yO_2$ compounds are shown in Figure 16 b). Note, that the Mg-doping content is y=0.08 for the compounds labeled with "h" and y=0.06 for the compounds labelled with "d". In contrast the experimentally synthesized compounds only exhibit a Mg content of y=0.05. In the case of the Mg free compounds in Figure 16 a) the O2 phase is starting to form at a Na content of 0.25 and is characterized by an invariant d-spacing indicating that the Na contents remains constant in line with the expected phase separation into filled P2 and empty O2. Note that several data points for the O2 and P2 phases in Fig. 16a lie on top of each other. The formation energy per formula unit calculated by DFT in Figure 15 a) show, that the structures at x=0.25 and x=0.33 are of very similar stability. In the case of the Mg-doped compounds in Figure 16 b) the formation of the Z-Phase is observed starting at a Na content of x=0.31 indicated in red. In contrast to the constant d-spacing in the O2 phase, the Z-phase is characterized by a constant evolution of the d-spacing with the Na content

x. As described above, the construction for the OP4 supercell for the defected honeycomb ordering results in a Na content x=0.17 while the OP4 supercell for the TM ordering with the optimal Ni-Ni distance contains a Na content x= 0.125. The resulting d-spacing for both TM orderings are in rather good agreement with the experimentally observed d-spacing for low Na contents, thus suggesting, that the OP4 structure could indeed be a major part of the Z-phase at high potentials.

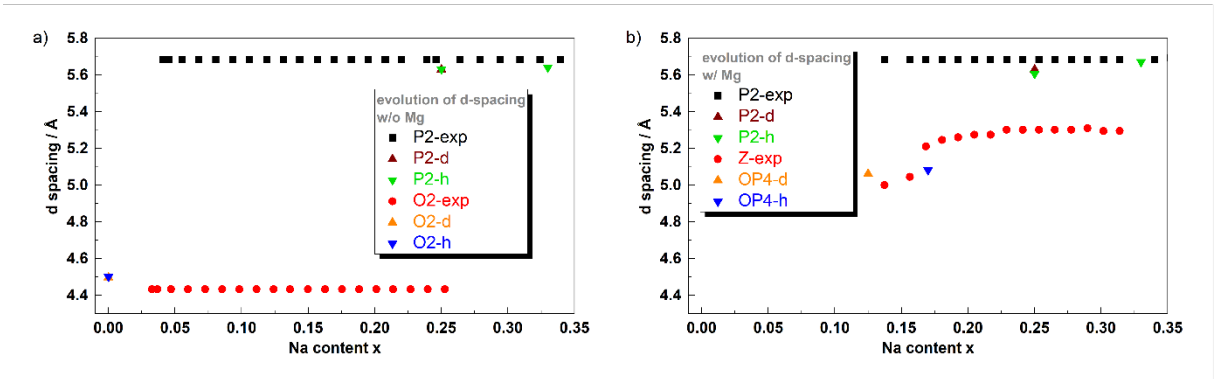

Figure 16: The evolution of the d spacing of the 002 reflection of the P2 and O2 structure and the 004 reflection of the OP4 structure upon the SPXRD measurement for the a) $Na_xMn_{0.75}Ni_{0.25}O_2$ compounds and the b) $Na_xMn_{0.75}Ni_{0.25-y}Mg_yO_2$ compounds in comparison with the d-spacing calculated by DFT. Calculations for the defected honeycomb TM ordering are labelled by the letter h, while the calculations for the TM ordering characterized by the optimized Ni-Ni distance are labelled by the letter d.

Conclusion

$P2\text{-}Na_{0.67}Mn_{0.75}Ni_{0.25-y}Mg_{0.05-x}O_2$ showed enhanced cyclability and rate performance in the potential range of 2-4.3 V vs Na/Na^+. The capacity retention was doubled after 100 galvanostatic cycles, with respect to the P2-NMO baseline material. Furthermore, P2-MNMO was also able to deliver a high CE, close to 99%. The doping with Mg led to a so-called 'Z-phase' like structure, in the range of 4.1 to 4.3 V vs Na/Na^+, which has been identified by means of SXRD measurements. Additional reflections for the O2-phase and 'Z-phase' were observed and compared with simulated XRD patterns (O2 and OP4), based on structures calculated by DFT. Furthermore, an asymmetric charge/discharge behaviour has been observed and investigated with *operando* SXRD. It was concluded that multiple phases dominate during the discharge at different SOCs. With GITT measurements, it was observed that Na^+ cation diffusivity could be highly improved with Mg as a doping agent (10^{-10} - 10^{-11} $cm^2\,s^{-1}$), in comparison to P2-MNO (10^{-11} - 10^{-13} $cm^2\,s^{-1}$) in the high potential area. DFT-calculated phase stabilities revealed that the experimentally observed formation of the "Z-phase" is due to the stabilization of the OP4 intermediate structure by Mg doping. The combined experimental and theoretical investigation of the phase transformation behavior in $P2\text{-}Na_{0.67}Mn_{0.75}Ni_{0.20}Mg_{0.05}O_2$ presented here provides new structural insights and can significantly contribute to the development of new Na ion cathode materials with improved specific capacity and rate capability.

Acknowledgements

This work contributes to the research performed at CELEST (Center for Electrochemical Energy Storage Ulm-Karlsruhe) and is funded by the Deutsche Forschungsgemeinschaft (DFG, German Research Foundation) under Project ID 390874152 (POLiS Cluster of Excellence) and by the German Federal Ministry of Education and Research (BMBF) in the project TRANSITION (03XP0186C). Our research work has gained benefit from beamtime allocation at BL04-MSPD at ALBA Synchrotron (2020094535-qfu), Barcelona, Spain. We appreciate Anna-Lena Hansen (IAM-ESS) for the helpful discussion regarding the Rietveld refinement and structural determination from *operando* synchrotron data. We also appreciate Oleksandr Dolotko (IAM-ESS) for the help with preliminary results of in-situ XRD measurements.

[1] M. Marinaro, D. Bresser, E. Beyer, P. Faguy, K. Hosoi, H. Li, J. Sakovica, K. Amine, M. Wohlfahrt-Mehrens, S. Passerini, *Journal of Power Sources* **2020**, *459*, 228073.
[2] a) B. L. Ellis, L. F. Nazar, *Current Opinion in Solid State and Materials Science* **2012**, *16*, 168; b) K. Kubota, N. Yabuuchi, H. Yoshida, M. Dahbi, S. Komaba, *MRS Bull.* **2014**, *39*, 416; c) V. Palomares, P. Serras, I. Villaluenga, K. B. Hueso, J. Carretero-González, T. Rojo, *Energy Environ. Sci.* **2012**, *5*, 5884; d) R. S. Carmichael, *Practical Handbook of Physical Properties of Rocks and Minerals*, CRC Press, **1989**; e) R. J. Clément, P. G. Bruce, C. P. Grey, *J. Electrochem. Soc.* **2015**, *162*, A2589-A2604.
[3] M. H. Han, E. Gonzalo, G. Singh, T. Rojo, *Energy Environ. Sci.* **2015**, *8*, 81.
[4] a) S. K. Sapra, J. Pati, P. K. Dwivedi, S. Basu, J.-K. Chang, R. S. Dhaka, *WIREs Energy Environ.* **2021**, *10*; b) H. Kim, H. Kim, Z. Ding, M. H. Lee, K. Lim, G. Yoon, K. Kang, *Adv. Energy Mater.* **2016**, *6*, 1600943; c) J. Zhang, W. Wang, W. Wang, S. Wang, B. Li, *ACS applied materials & interfaces* **2019**, *11*, 22051.
[5] C. Delmas, C. Fouassier, P. Hagenmuller, *Physica 99B* **1980**, 81.
[6] A. Gutierrez, W. M. Dose, O. Borkiewicz, F. Guo, M. Avdeev, S. Kim, T. T. Fister, Y. Ren, J. Bareño, C. S. Johnson, *J. Phys. Chem. C* **2018**, *122*, 23251.
[7] C. Delmas, C. Fouassier, P. Hagenmuller, *Physica 99B* **1980**, 81.
[8] S. Komaba, N. Yabuuchi, T. Nakayama, A. Ogata, T. Ishikawa, I. Nakai, *Inorganic chemistry* **2012**, *51*, 6211.
[9] K. Kubota, S. Kumakura, Y. Yoda, K. Kuroki, S. Komaba, *Adv. Energy Mater.* **2018**, *8*, 1703415.
[10] a) C. Delmas, J.-J. Braconnier, C. Fouassier, P. Hagenmuller, *Solid State Ionics 3/4* **1981**, 165; b) K. Kubota, S. Komaba, *J. Electrochem. Soc.* **2015**, *162*, A2538-A2550.
[11] Y. Zhang, R. Zhang, Y. Huang, *Frontiers in chemistry* **2019**, *7*, 335.
[12] N. Ortiz-Vitoriano, N. E. Drewett, E. Gonzalo, T. Rojo, *Energy Environ. Sci.* **2017**, *10*, 1051.
[13] a) R. J. Clément, P. G. Bruce, C. P. Grey, *J. Electrochem. Soc.* **2015**, *162*, A2589-A2604; b) S. Guo, H. Yu, Z. Jian, P. Liu, Y. Zhu, X. Guo, M. Chen, M. Ishida, H. Zhou, *ChemSusChem* **2014**, *7*, 2115.
[14] a) S. Kumakura, Y. Tahara, K. Kubota, K. Chihara, S. Komaba, *Angew. Chem.* **2016**, *128*, 12952; b) B. Mortemard de Boisse, G. Liu, J. Ma, S.-I. Nishimura, S.-C. Chung, H. Kiuchi, Y. Harada, J. Kikkawa, Y. Kobayashi, M. Okubo et al., *Nature communications* **2016**, *7*, 11397; c) T. Jin, P.-F. Wang, Q.-C. Wang, K. Zhu, T. Deng, J. Zhang, W. Zhang, X.-Q. Yang, L. Jiao, C. Wang, *Angewandte Chemie (International ed. in English)* **2020**, *59*, 14511; d) G. J. Shu, F. C. Chou, *Phys. Rev. B* **2008**, *78*; e) Z. Lu, J. R. Dahn, *J. Electrochem. Soc.* **2001**, *148*, A1225.
[15] A. Konarov, J. U. Choi, Z. Bakenov, S.-T. Myung, *J. Mater. Chem. A* **2018**, *6*, 8558.
[16] a) L. Zheng, J. Li, M. N. Obrovac, *Chem. Mater.* **2017**, *29*, 1623; b) D. Yuan, X. Hu, J. Qian, F. Pei, F. Wu, R. Mao, X. Ai, H. Yang, Y. Cao, *Electrochimica Acta* **2014**, *116*, 300; c) D. Yuan, W. He, F. Pei, F. Wu, Y. Wu, J. Qian, Y. Cao, X. Ai, H. Yang, *J. Mater. Chem. A* **2013**, *1*, 3895; d) Q.-C. Wang, J.-K. Meng, X.-Y. Yue, Q.-Q. Qiu, Y. Song, X.-J. Wu, Z.-W. Fu, Y.-Y. Xia, Z. Shadike, J. Wu et al., *Journal of the American Chemical Society* **2019**, *141*, 840.
[17] G. Singh, N. Tapia-Ruiz, J. M. Del Lopez Amo, U. Maitra, J. W. Somerville, A. R. Armstrong, J. Martinez de Ilarduya, T. Rojo, P. G. Bruce, *Chem. Mater.* **2016**, *28*, 5087.
[18] N. Tapia-Ruiz, W. M. Dose, N. Sharma, H. Chen, J. Heath, J. W. Somerville, U. Maitra, M. S. Islam, P. G. Bruce, *Energy Environ. Sci.* **2018**, *11*, 1470.
[19] H. Hou, B. Gan, Y. Gong, N. Chen, C. Sun, *Inorganic chemistry* **2016**, *55*, 9033.

[20] N. Yabuuchi, M. Kajiyama, J. Iwatate, H. Nishikawa, S. Hitomi, R. Okuyama, R. Usui, Y. Yamada, S. Komaba, *Nature materials* **2012**, *11*, 512.
[21] B. Mortemard de Boisse, D. Carlier, M. Guignard, L. Bourgeois, C. Delmas, *Inorganic chemistry* **2014**, *53*, 11197.
[22] J. W. Somerville, A. Sobkowiak, N. Tapia-Ruiz, J. Billaud, J. G. Lozano, R. A. House, L. C. Gallington, T. Ericsson, L. Häggström, M. R. Roberts et al., *Energy Environ. Sci.* **2019**, *12*, 2223.
[23] L. F. Pfeiffer, N. Jobst, C. Gauckler, M. Lindén, M. Marinaro, S. Passerini, M. Wohlfahrt-Mehrens, P. Axmann, *Front. Energy Res.* **2022**, *10*.
[24] J. Rodríguez-Carvajal, *Newsletter* **2001**, 12.
[25] a) P. Hohenberg and W. Kohn, *physical review* **1964**, *136*, B864; b) W. Kohn and L. J. Sham, *physical review* **1965**, 1134-1138.
[26] a) John P. Perdew, Kieron Burke, Matthias Ernzerhof, *Physical Review Letters* **1996**, 3865; b) S. Grimme, S. Ehrlich, L. Goerigk, *Journal of computational chemistry* **2011**, *32*, 1456.
[27] a) P. E. Blöchl, *Phys. Rev. B* **1994**, 17653; b) G. Kresse and J. Hafner, *Phys. Rev. B* **1993**, 558; c) Kresse, Furthmüller, *Physical review. B, Condensed matter* **1996**, *54*, 11169; d) G. Kresse, D. Joubert, *Phys. Rev. B* **1999**, *59*, 1758.
[28] L. Wang, T. Maxisch, G. Ceder, *Phys. Rev. B* **2006**, *73*.
[29] a) K. Kaliyappan, W. Xaio, T.-K. Sham, X. Sun, *Adv. Funct. Mater.* **2018**, *28*, 1801898; b) J. Ying, M. Lei, C. Jiang, C. Wan, X. He, J. Li, L. Wang, J. Ren, *Journal of Power Sources* **2006**, *158*, 543.
[30] a) Jaephil Cho, Geunbae Kim, Hong Sup Lim, *Journal of The Electrochemical Society* **1999**, *146*, 3571; b) J. Ying, C. Jiang, C. Wan, *Journal of Power Sources* **2004**, *129*, 264; c) X. Luo, X. Wang, L. Liao, S. Gamboa, P. J. Sebastian, *Journal of Power Sources* **2006**, *158*, 654; d) M. Xiang, W. Tao, J. Wu, Y. Wang, H. Liu, *Ionics* **2016**, *22*, 1003.
[31] H.-J. Kim, H.-G. Jung, B. Scrosati, Y.-K. Sun, *Journal of Power Sources* **2012**, *203*, 115.
[32] a) I. Hasa, D. Buchholz, S. Passerini, J. Hassoun, *ACS applied materials & interfaces* **2015**, *7*, 5206; b) R. Luo, F. Wu, M. Xie, Y. Ying, J. Zhou, Y. Huang, Y. Ye, L. Li, R. Chen, *Journal of Power Sources* **2018**, *383*, 80.
[33] S.-Y. Xu, X.-Y. Wu, Y.-M. Li, Y.-S. Hu, L.-Q. Chen, *Chinese Phys. B* **2014**, *23*, 118202.
[34] X. Chen, N. Li, E. Kedzie, B. D. McCloskey, H. Tang, W. Tong, *J. Electrochem. Soc.* **2019**, *166*, A4136-A4140.
[35] W. Weppner, R. A. Huggins, *The Electrochemical Society* **1977**, 1569.
[36] E. Markevich, M. D. Levi, D. Aurbach, *Journal of Electroanalytical Chemistry* **2005**, *580*, 231.
[37] Y. Zhu, C. Wang, *J. Phys. Chem. C* **2010**, *114*, 2830.
[38] Balsys R. J., Davies R. L., *Solid State Ionics* **1994**, 69.
[39] J. M. Paulsen, J. R. Dahn, *Solid State Ionics* **1999**, 3.
[40] a) R. Berthelot, M. Pollet, D. Carlier, C. Delmas, *Inorganic chemistry* **2011**, *50*, 2420; b) Y. Biecher, D. L. Smiley, M. Guignard, F. Fauth, R. Berthelot, C. Delmas, G. R. Goward, D. Carlier, *Inorganic chemistry* **2020**, *59*, 5339.
[41] K. Momma, F. Izumi, *J Appl Crystallogr* **2008**, *41*, 653.
[42] Y. Zhang, M. Wu, J. Ma, G. Wei, Y. Ling, R. Zhang, Y. Huang, *ACS central science* **2020**, *6*, 232.
[43] a) J. H. Chang, D. Kleiven, M. Melander, J. Akola, J. M. Garcia-Lastra, T. Vegge, *Journal of physics. Condensed matter : an Institute of Physics journal* **2019**, *31*, 325901; b) A. van de Walle, M. Asta, G. Ceder, *Calphad* **2002**, *26*, 539.
[44] a) Z. Lu, R. A. Donaberger, J. R. Dahn, *Chem. Mater.* **2000**, *12*, 3583; b) R. A. House, U. Maitra, M. A. Pérez-Osorio, J. G. Lozano, L. Jin, J. W. Somerville, L. C. Duda, A. Nag, A. Walters, K.-J. Zhou et al., *Nature* **2020**, *577*, 502.
[45] D. H. Lee, J. Xu, Y. S. Meng, *Physical chemistry chemical physics : PCCP* **2013**, *15*, 3304.

TOC

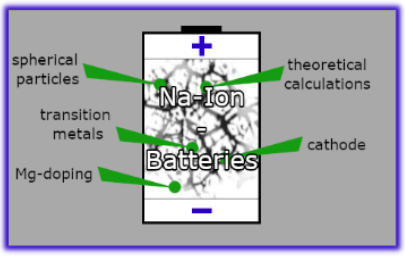

This publication aims at addressing the improvement of Mg-doped Mn/Ni based transition metal cathode material for Na+ Ion batteries by combining experimental investigation and theoretical calculations.